PAPER • OPEN ACCESS

Controlling photocurrent channels in scanning tunneling microscopy

To cite this article: Benjamin Schröder *et al* 2020 *New J. Phys.* **22** 033047

View the article online for updates and enhancements.

New Journal of Physics
The open access journal at the forefront of physics

CrossMark

PAPER

Controlling photocurrent channels in scanning tunneling microscopy

Benjamin Schröder [orcid] , Ole Bunjes [orcid] , Lara Wimmer[1] [orcid] , Katharina Kaiser[2] [orcid] , Georg A Traeger [orcid] , Thomas Kotzott [orcid] , Claus Ropers[3] [orcid] and Martin Wenderoth[3] [orcid]

4th Physical Institute-Solids and Nanostructures, University of Göttingen, D-37077, Göttingen, Germany
[1] Current address: IHP—Leibniz-Institut für innovative Mikroelektronik, D-15236, Frankfurt (Oder), Germany.
[2] Current address: IBM Research–Zürich, 8803 Rüschlikon, Switzerland.
[3] Authors to whom any correspondence should be addressed.

E-mail: claus.ropers@uni-goettingen.de and martin.wenderoth@uni-goettingen.de

Abstract

We investigate photocurrents driven by femtosecond laser excitation of a (sub)-nanometer tunnel junction in an ultrahigh vacuum low-temperature scanning tunneling microscope (STM). The optically driven charge transfer is revealed by tip retraction curves showing a current contribution for exceptionally large tip-sample distances, evidencing a strongly reduced effective barrier height for photoexcited electrons at higher energies. Our measurements demonstrate that the magnitude of the photo-induced electron transport can be controlled by the laser power as well as the applied bias voltage. In contrast, the decay constant of the photocurrent is only weakly affected by these parameters. Stable STM operation with photoelectrons is demonstrated by acquiring constant current topographies. An effective non-equilibrium electron distribution as a consequence of multiphoton absorption is deduced by the analysis of the photocurrent using a one-dimensional potential barrier model.

Introduction

The combination of ultrafast laser pulses with scanning tunneling microscopy (STM) promises advancements in surface science by connecting sub-nanometer resolution with light-driven dynamics [1–5]. Various optically induced phenomena have been investigated on an atomic level, such as surface photochemical reactions [6–13], photo-induced molecular motion [14–19], charging of individual molecules, defects, dopants and nanostructures [20–26], and tip-enhanced Raman scattering by nanostructures and single molecules [27–32]. Time-resolved STM operation gains particular attention in the form of pump-probe excitation of dynamical processes, which can reach the femtosecond (fs) domain [9, 16, 21–23, 25, 33–39].

Light emission from the tunnel gap is exploited to investigate inelastic electron transport across the tip-sample contact, such as the radiative decay of localized plasmons [40–44], mapping of molecular orbitals [45], as well as time-resolved and time-correlated electroluminescence [46–48]. The inverse process—exciting the tunnel junction by photons—involves several experimental complications. Particularly, the temperature modulation accompanied by pulsed illumination results in junction instabilities, often obscuring the signals or preventing atomic resolution, as investigated in [1, 49]. Recent technological developments, including the application of THz transients [16, 33], shaken pulse-pair excitation (SPPX) [50, 51], two-color SPPX [52, 53], two-pulse picking [22, 23] and cross-polarized double beat methods [54, 55] have led to a reliable laser coupling to STM. Further near-field schemes, such as plasmonic nanofocusing, have the potential to further enhance the coupling to the tunneling gap [56–60].

Alongside this instrumental progress, a detailed understanding of the properties of a tunnel contact during and after fs-laser illumination remains of interest, involving linear and nonlinear absorption mechanisms, transient modifications of the local field distribution, and the diverse pathways of excited charge carriers.

Specifically, the energetic distribution of the tunneling electrons due to the optical excitation and the roles of different photocurrent channels is of particular relevance.

In this work, we study the generation of photocurrents by fs-laser pulses in an ultrahigh vacuum (UHV) low-temperature STM. The light-driven electron transport manifests itself in modified current-distance dependencies characterized by a much larger decay length compared to regular tunneling. While the magnitude of the photocurrent can be controlled by the incident laser power and the bias voltage, its decay length is largely unaffected by these parameters. Thus, the size of the tunneling gap can be used to vary the ratio of regular tunneling to optically driven electron transfer which allows for stable laser based constant-current imaging of a Cu(100) surface. The observed decay lengths of the photocurrent cannot be directly attributed to the spatially dependent field enhancement of a plasmonic gap mode. In order to identify the mechanism underlying of these enhanced photocurrents, we performed simulations based on a one-dimensional transport model and an effective electron occupation. From these simulations, we identify the major contribution to the photocurrent with transfer channels for hot electrons with energies near the potential barrier maximum.

Methods

The experiments were performed with a home-built UHV low-temperature STM at a base pressure of 5×10^{-11} mbar and a base temperature of 80 K. Depending on the chosen bandwidth of the measurement electronics and the stability of the tip-sample contact, a current resolution of 50–200 fA is achieved in our setup. The bias voltage U_B is applied to the sample while the tip is virtually connected to ground via the current amplifier. Electrochemically etched gold tips and a Cu(100) crystal have been utilized as the probe and surface material, respectively (figure 1(a)).

A mode-locked Ti:Sapphire laser oscillator with a center wavelength of 785 nm and 80 MHz repetition rate is used for optical excitation. Pulse duration and focus diameter in the STM chamber are estimated to 70 fs and 18 μm full-width at half-maximum (FWHM) (see appendix 'Interferometric autocorrelation'). The light polarization was chosen to be aligned along the tip's symmetry axis (unless otherwise stated). An overlap of the tunnel contact and the laser focus is achieved by a plano-convex lens ($f = 200$ mm) mounted outside the STM chamber on a 3D-translation stage (see focal raster scan in the left inset of figure 1(c)). The optical table and floating STM platform are mechanically decoupled; relative movements of the focus to the tunnel gap are compensated by an active beam stabilization system. Experimental details are found in the appendix 'Methods'.

Experiments

The fundamental ability of resolving single atoms in STM is based on the exponential decay of the tunnel current I upon retracting the tip by the displacement z from the sample. For our system—without illumination—a standard $I(z)$ curve is plotted in figure 1(b) (black line)[4] showing a slope of 0.8 decades per Ångström, corresponding to an apparent barrier height (ABH) of 3.2 eV for the tunneling electrons (for a definition of the ABH see appendix 'Apparent barrier height'). With a setpoint current of $I_{SP} = 500$ pA, the tunnel current drops below a noise level upon retracting the tip by ∼0.5 nm.

A striking change of the retraction curves is observed when the junction is illuminated with fs-laser pulses (figure 1(b), red to yellow lines). Whereas the current closely follows the (unilluminated) reference at small distances, illumination of the gap greatly enhances the current for increasing displacements. For these larger displacements, the curves again decay as a single exponential. Increasing the laser power to 4.3 mW the photo-driven contribution raises to the 100 fA level up to a distance of 2.3 nm.

We describe the distance-dependent current as the sum of a regular tunneling contribution and a photocurrent, fitting the expression

$$I_{\text{total}}(z_0 + z) = I_{SP} \cdot \exp(-2\kappa_{\text{tc}}z) + I_{\text{pc}} \cdot \exp(-2\kappa_{\text{pc}}z) \tag{1}$$

to the experimental data, where z_0 is the tip-sample distance at which the setpoint is reached without laser illumination. We extract the photo-driven current fraction (I_{pc}/I_{SP}), regular tunnel current ABH $\Phi_{\text{tc}} = \hbar^2 \kappa_{\text{tc}}^2 / 2m_e$ and photocurrent ABH $\Phi_{\text{pc}} = \hbar^2 \kappa_{\text{pc}}^2 / 2\,m_e$ from the obtained decay constants (m_e is the electron mass).

For the regular tunneling contribution, we find the ABH to be independent of the applied laser power; the value of $\Phi_{\text{tc}} \sim 3.2$ eV agrees well with that of the reference curve. In contrast, the ABH of the photo-induced

---

[4] Note that throughout this paper, the given displacements z are relative to a starting point $z_0(U_B = 2 \text{ V}, I_{SP})$, i.e. the initial tip-sample distance, defined by the bias voltage U_B (set to 2 V) and the set point current I_{SP} without laser illumination. Usually, z_0 attains values between 0.7 and 0.9 nm for typical tunnel parameters [61]. Additionally, z_0 must be modified by $\Delta z(U_B, P)$ when changing the bias voltage or laser power (see appendix 'Start point correction').
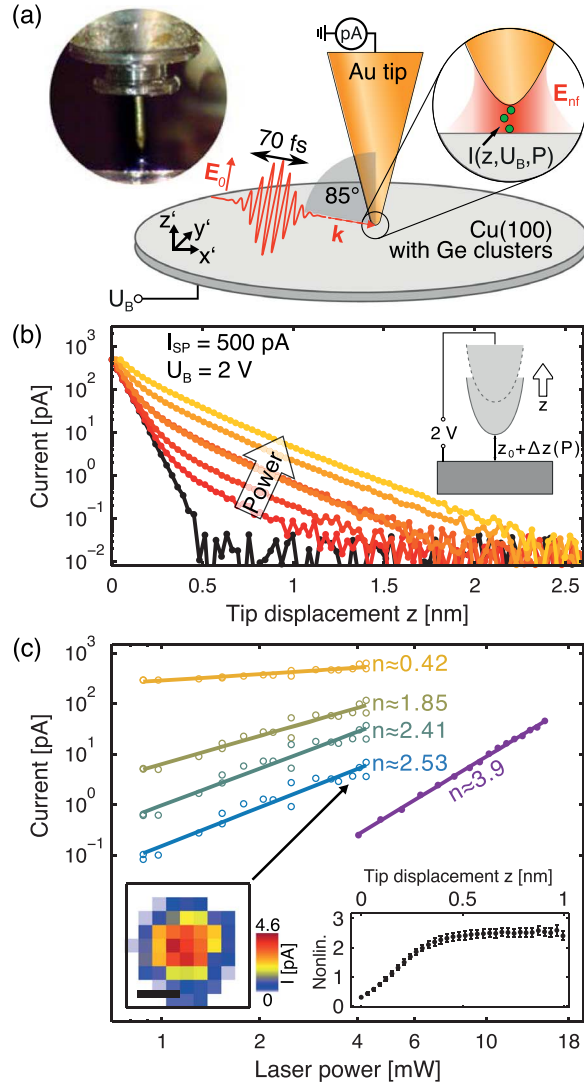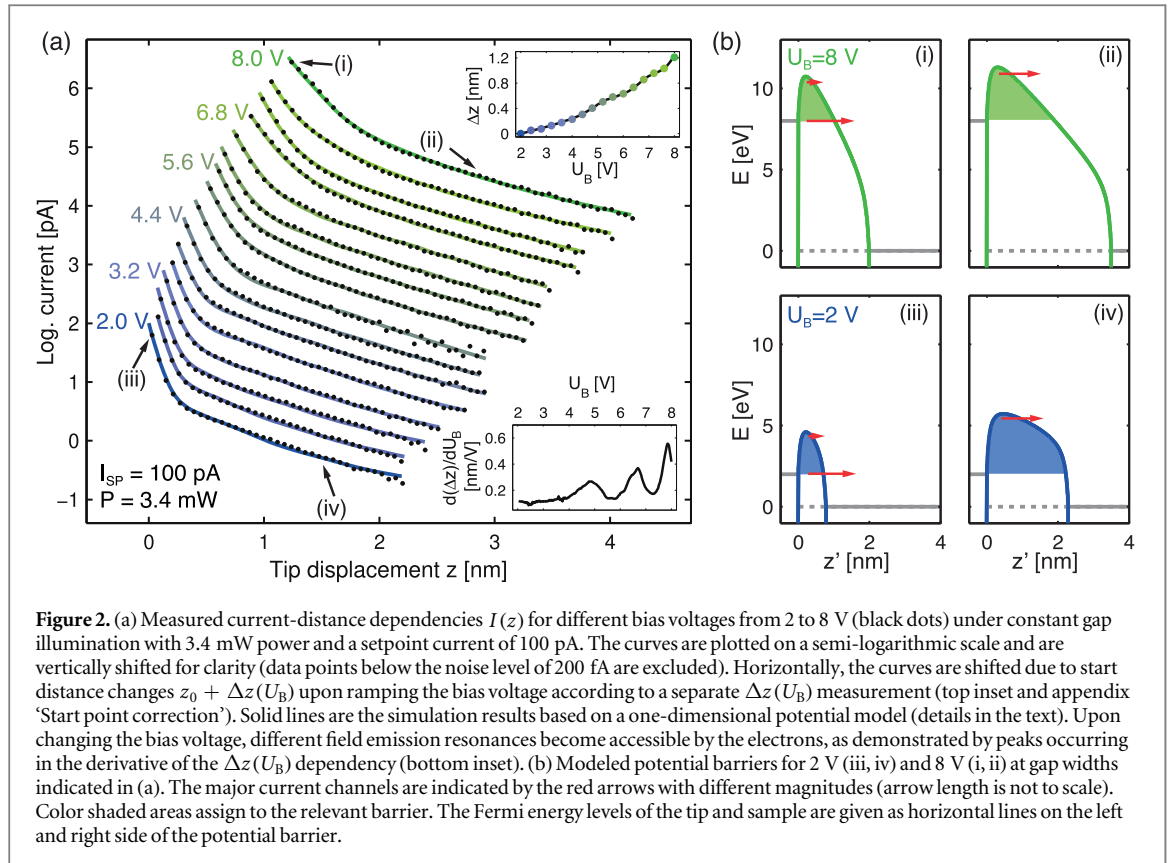
Figure 1. (a) Schematic illustration of the experimental setup. A gold tip and Cu(100) surface are used as probe and sample, respectively. The p-polarized laser field ($\mathbf{E_0}$) propagating with the wave vector $\mathbf{k}$ is focused onto the tunnel contact (see photo). Generally, the measured current is a function of gap width, bias voltage and laser power (indicated in the zoom-in). Laser illumination leads to an enhanced near-field $\mathbf{E_{nf}}$ in the tunnel junction. (b) Current-distance dependencies without (black dots) and with gap illumination (increasing power from red to yellow dots: 1.0, 1.3, 1.8, 2.5, 3.3 and 4.3 mW) (logarithmic scale). The inset schematically demonstrates the measurement: Starting from the setpoint of 500 pA reached at $z_0 + \Delta z(P)$, the tip is retracted while measuring the current. (c) Double-logarithmic plot of the current as a function of average laser power for different tip displacements (0.03, 0.3, 0.5, and 0.9 nm (yellow to blue)). The effective nonlinearities n resulting from linear fits (solid lines) are indicated near the curves. For comparison, the current-power dependency of the tip retracted ~1 μm from the surface is plotted in purple. (Right inset) Nonlinearity as a function of tip displacement. For $z > 0.5$ nm the nonlinear order attains a nearly constant value of ~2.5. (Left inset) Focal raster scan across the tunnel gap for a tip displacement of 0.9 nm (scale bar: 5 μm) demonstrating a more strongly confined photocurrent (~20 μm^2) than the focus spot size (~250 μm^2).

current is $\Phi_{pc} \sim 0.2$ eV. Interestingly, it also shows no dependency on the laser power. The 16 fold reduction of the ABH is an indication of tunneling electrons excited to higher energy levels, close to the vacuum edge. The fraction of the photocurrent prefactors I_{pc}/I_{SP} changes from <1% for the lowest to 60% for the highest measured laser power. Due to the additional photocurrent, for laser illumination, the setpoint is established at an offset distance $\Delta z(P) > 0$ from z_0, determined from the condition $I_{total}(z_0 + \Delta z(P)) = I_{SP}$ (see appendix 'Start point correction'). Note that these offsets are of minor magnitude.

The high stability of our setup allows for an investigation of the nonlinearity of the photocurrent (figure 1(c)). As reference, we measured the photo-emitted current for the retracted tip (~1 μm distance to the sample). Laser-driven electron currents from free-standing gold tips previously revealed multiphoton photoemission (MPPE) processes [58, 62–66]. This is described by a generalized Fowler–DuBridge theory connecting the current with the average laser power P by a power law, $I \sim P^n$ [67]. The effective nonlinear order n is a measure of the number of photons per electron involved in the photoemission process. We observe a nonlinearity of 3.9 (purple dots), close to the expected value for an Au tip with a work function of ~5 eV.

Figure 2. (a) Measured current-distance dependencies $I(z)$ for different bias voltages from 2 to 8 V (black dots) under constant gap illumination with 3.4 mW power and a setpoint current of 100 pA. The curves are plotted on a semi-logarithmic scale and are vertically shifted for clarity (data points below the noise level of 200 fA are excluded). Horizontally, the curves are shifted due to start distance changes $z_0 + \Delta z(U_B)$ upon ramping the bias voltage according to a separate $\Delta z(U_B)$ measurement (top inset and appendix 'Start point correction'). Solid lines are the simulation results based on a one-dimensional potential model (details in the text). Upon changing the bias voltage, different field emission resonances become accessible by the electrons, as demonstrated by peaks occurring in the derivative of the $\Delta z(U_B)$ dependency (bottom inset). (b) Modeled potential barriers for 2 V (iii, iv) and 8 V (i, ii) at gap widths indicated in (a). The major current channels are indicated by the red arrows with different magnitudes (arrow length is not to scale). Color shaded areas assign to the relevant barrier. The Fermi energy levels of the tip and sample are given as horizontal lines on the left and right side of the potential barrier.

For different tips, we find values of n between 3.5 and 4.5, consistent with earlier results for free-standing tips [58, 62, 64]. For the tip-sample contact, the nonlinear order is greatly suppressed: n attains a constant value of ~2.5 for all displacements $z > 0.5$ nm (right inset in figure 1(c)), which is in accordance with a previous result [36]. Importantly, this nonlinearity indicates lower-order emission processes for the photon-driven current contribution compared to the free-standing tip. For $z < 0.5$ nm (green and yellow line), the found values are further reduced by the additional regular tunneling, which starts to dominate upon approaching the setpoint. Hence, this reduction in nonlinearity is not linked to a change of the electron transfer process. Interferometric autocorrelation measurements of the photocurrents emitted from a free-standing tip and in the tunnel contact confirmed the general trend of a reduced nonlinear order for the gap illumination (see appendix 'Interferometric autocorrelation').

The reduced barrier involved in the photo-induced electron transfer suggests a further investigation of the photocurrent dependency on the barrier shape and height, which can be adjusted by the bias voltage (figure 2(a)). While the data at a low bias voltage ($U_B < 5$ V) can be described by the above-mentioned bi-exponential behavior, additional features are observed for $U_B > 5$ V. These are attributed to field emission resonances (FER), also evident as peaks in the $d(\Delta z)/dU_B$ spectrum [68–71] (bottom inset of figure 2(a)) (details are found in the appendix 'Field emission resonances'). For measurements in the interval from 2 to 8 V, we extract regular tunneling ABHs ranging from 3.0 eV down to 0.5 eV, respectively. These values match to the found Φ_{tc} without illumination (a comparison of dark versus illuminated data is given in figure A3 in the appendix 'Bias voltage dependent measurements'). Interestingly, the determined ABHs of the photocurrents do not exhibit such a trend, with values weakly varying around a few to a few tens of meV.

The transition to the negative bias voltages regime (-1 V $\leqslant U_B \leqslant 0$ V) reveals positive, photo-driven currents (figure A4 in the appendix 'Bias voltage dependent measurements'): Although the negative setpoint results in a negative regular tunneling (from the sample to the tip) for very small displacements, we find optically driven electron transfer reverse to the static electric field (from the tip to the sample) for larger tip displacements. Note that for $U_B \lesssim -1$ V the positive photocurrent is compensated by negative photo-driven currents from the surface.

Laser-driven STM

Controlling the photocurrent fraction I_{pc}/I_{SP} allows for a transition from regular to photon based imaging. To investigate the impact of surface features on the photocurrent and on topographic information, we measured
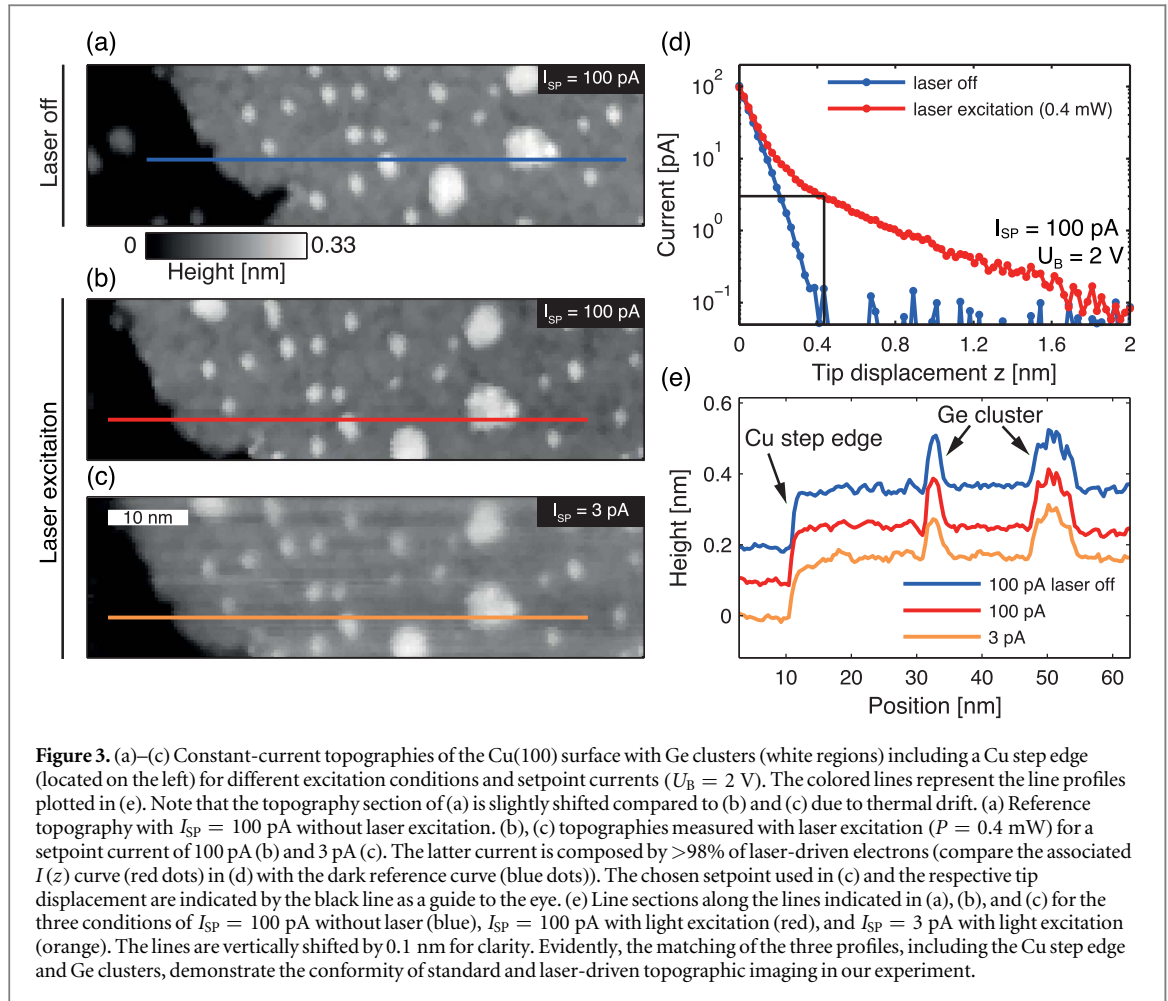
Figure 3. (a)–(c) Constant-current topographies of the Cu(100) surface with Ge clusters (white regions) including a Cu step edge (located on the left) for different excitation conditions and setpoint currents ($U_B = 2$ V). The colored lines represent the line profiles plotted in (e). Note that the topography section of (a) is slightly shifted compared to (b) and (c) due to thermal drift. (a) Reference topography with $I_{SP} = 100$ pA without laser excitation. (b), (c) topographies measured with laser excitation ($P = 0.4$ mW) for a setpoint current of 100 pA (b) and 3 pA (c). The latter current is composed by >98% of laser-driven electrons (compare the associated $I(z)$ curve (red dots) in (d) with the dark reference curve (blue dots)). The chosen setpoint used in (c) and the respective tip displacement are indicated by the black line as a guide to the eye. (e) Line sections along the lines indicated in (a), (b), and (c) for the three conditions of $I_{SP} = 100$ pA without laser (blue), $I_{SP} = 100$ pA with light excitation (red), and $I_{SP} = 3$ pA with light excitation (orange). The lines are vertically shifted by 0.1 nm for clarity. Evidently, the matching of the three profiles, including the Cu step edge and Ge clusters, demonstrate the conformity of standard and laser-driven topographic imaging in our experiment.

constant-current topographies of a Cu(100) surface covered with 0.1–0.2 monolayers of Ge clusters (figure 3). By controlling the setpoint current and laser illumination, we can change the ratio I_{pc}/I_{SP} (figure 3(d)). Interestingly, both measurements with laser excitation for $I_{pc}/I_{SP} = 8\%$ (b) and $I_{pc}/I_{SP} = 98\%$ (c) resolve all features present in the reference topography without illumination (a) (there is a small thermally induced drift). Some blurring in (c) is attributed to the increased tip-sample distance (broader transfer function of the tip). Figure 3(e) demonstrates for all three scenarios (standard tunneling, $I_{pc}/I_{SP} = 8\%$, and $I_{pc}/I_{SP} = 98\%$) a quantitative agreement of the topographic heights of the Cu step edge and the Ge clusters.

We note that multiple sequentially measured topographies with and without laser illumination show no indication of a tip- or laser-induced surface modification. We can therefore rule out previously observed changes in surface morphology [72], induced by thermal tip expansion and penetration into the surface [1, 73, 74].

Modeling

In the following, we address the mechanism underlying the observed current-distance characteristics $I(z)$ for the optically excited tunnel junction. Generally, the electron transport is determined by two major quantities. Firstly, the charge carrier has a transfer probability T to transmit from one electrode to the other. Specifically, T is determined by the potential barrier formed between both electrodes. Hence, it is a function of the electron energy E, the gap width $z_{gap} \sim z$ and the bias voltage U_B. Secondly, the number of transmitting charge carriers is given by the initial occupied and by the final empty states. In an elastic process, this number is a function of the occupation distribution and density of states of the tip and sample at the energy E [61].

Under fs-laser excitation both the transmission probability and the electron population can be transiently changed due to photon absorption or local field modifications. However, for moderate excitation intensities (perturbative regime), we can exclude strong-field effects on the potential landscape determining the transmission probability (see discussion) [36, 64]. Therefore, the impact of the laser excitation on the electron population can be modeled by an effective time-averaged occupation function f_{eff} [62, 75].

Based on the Bardeen model for tunneling, we calculate the current I by an energy (E) integral over the product of the electron occupation f_{eff} and the transmission probability T [61]:

$$I(z, \ U_B, \ \mathbf{E}_{nf}) \sim \int_0^\infty f_{eff}(E, \ E_{nf}(z)) \cdot T(E, \ z, \ U_B)\, dE, \tag{2}$$

assuming a constant density of states for the tip and the sample. The temperature of the sample is set to 0 K, hence, the electron occupation is unity up to the Fermi level on the sample side. Importantly, the electron population in the tip f_{eff} is given by the absorption of photons from the enhanced near-field $\mathbf{E}_{nf}$ in the tunnel gap (see zoom-in in figure 1(a)), which depends on the laser power, the tip-sample geometry and the dielectric response of the materials. Especially, for gold nanostructures excited with near-infrared light, we expect a strong enhancement of $\mathbf{E}_{nf}$ due to a local surface plasmon (gap plasmon) [29, 41, 76, 77]. Explicitly, both the occupation f_{eff} and transmission T are functions of the tip-sample distance $z_{gap} \sim z$, which is given by the tip displacement z in the experiment.

We first consider the possibility of the local field $\mathbf{E}_{nf}(z)$ responsible for the measured photocurrent spatial decay. Since the plasmonic enhancement is a function of the system's geometry and the dielectric properties of the materials, a strong modification of $\mathbf{E}_{nf}$ is expected when sharp features on the surface or different materials are present in the gap [55, 60, 77–79]. This should lead to different topographic heights when imaging the surface with photo-driven electrons compared to the regular tunneling. Yet, we find the same topographic profiles for both cases (see figure 3(c)).
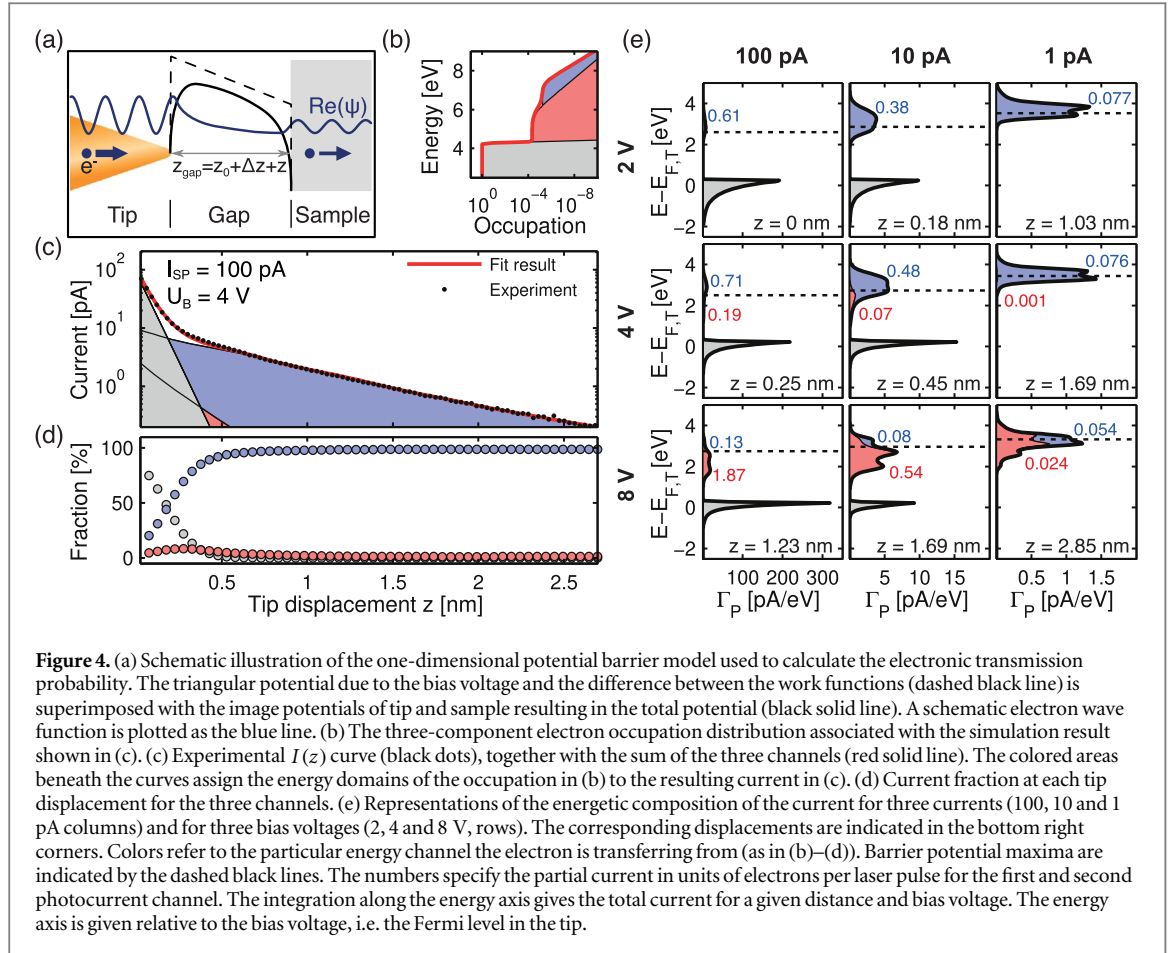
Moreover, given the experimental geometry, the very short decay lengths render the gap plasmon z-dependency an unlikely explanation. Specifically, the expected field-distance dependency of the signal can be estimated by a coupled dipole approximation, with the tip apex modeled as a sphere (see appendix 'Near-field enhancement') [80]. The associated electric field component in the z'-direction E_{nf} is given by an algebraic relation $E_{nf} \sim (z_{gap} + R_T)^{-3}$ with the tip radius R_T and gap width $z_{gap} \sim z$ [29]. Estimating the distance dependency of a current driven by a nonlinear process ($I(z) \sim |E_{nf}(z)|^{2n}$) for different tip radii and $n = 2.5$ (figure A6 in the appendix 'Near-field enhancement'), the observed decay lengths in our experiment could only be achieved for unrealistically small tip radii ($\lesssim 5$ nm). However, such radii would lead to a strong deviation from an exponential law, in contrast to our experimental findings. We estimate a signal reduction by a factor of up to ~11 in the experimentally relevant regime of 0.7–3.2 nm for a tip radius providing a nearly exponential decay of the near-field (the actual reduction factor is expected to be even lower, since plasmon-driven tunneling reduces the field enhancement for very low distances [29, 81]). In contrast, we find reduction factors of up to 10^4 in the related distance regime in our experiment (see figure 1(c)). Interestingly, a current-distance dependency measured for increased laser powers (~35 mW) strongly deviates from the low-power experiments (figure A7 in the appendix 'Near-field enhancement'). The setpoint current is purely laser-driven. Therefore, the tip-sample distance must be considerably larger[5]. In this case, it deviates from an exponential law with a decay length much larger compared to the curves in figure 1(b) and figure 2(a), and the current converges to a finite value of 0.4 pA at the distance of 10 nm. A tip radius of $R_T = 28$ nm and a nonlinear order of $n = 4.4$ is extracted from a fit of the coupled dipole model to the data in figure A7. We attribute these results to a four-photon process dominating the intermediate distance regime with a current decay governed by $\mathbf{E}_{nf}(z)$. Thus, another mechanism must be responsible for the observed decay length scale for the short distance regime and the near-field enhancement is assumed to be constant in the model discussed below. Consequently, the effective occupation distribution has only an explicit energy dependency, whereas the near-field enters as a parameter given by the laser power ($f_{eff}(E, \ \mathbf{E}_{nf}) = f_P(E)$).

We find the z-dependency of the transmission probability $T(E, \ z, \ U_B)$ to explain the observed photocurrent spatial decay. We calculate T with a one-dimensional representation of the potential landscape including image potentials for both electrodes (figure 4(a) and panels (i)–(iv) in figure 2(b)). Field emission resonances and their spectral change due to the Stark shift is covered by the model as well. For this potential, we numerically solve the Schrödinger equation with the Numerov method (see schematic wave function in figure 4(a)) and extract the transmission probability from the found scattering parameters [82, 83]. A detailed description is found in the appendix 'Transport model'. From equation (2) the current with its tip-sample distance and bias voltage dependency is simulated as a function of the excited electron population $f_P(E)$,

$$I(z, \ U_B) = C \int_0^\infty f_P(E) \cdot T(E, \ z, \ U_B)\, dE, \tag{3}$$

with a scaling constant C. $f_P(E)$ is modeled as a parameterized sum over N Fermi–Dirac distributions of different magnitudes A_j, energy intervals E_j and energy widths ΔE_j [62, 75]:

---

[5] A precise start distance cannot be given, since no reference in the form of a transition starting from regular tunneling is present in the data.

Figure 4. (a) Schematic illustration of the one-dimensional potential barrier model used to calculate the electronic transmission probability. The triangular potential due to the bias voltage and the difference between the work functions (dashed black line) is superimposed with the image potentials of tip and sample resulting in the total potential (black solid line). A schematic electron wave function is plotted as the blue line. (b) The three-component electron occupation distribution associated with the simulation result shown in (c). (c) Experimental $I(z)$ curve (black dots), together with the sum of the three channels (red solid line). The colored areas beneath the curves assign the energy domains of the occupation in (b) to the resulting current in (c). (d) Current fraction at each tip displacement for the three channels. (e) Representations of the energetic composition of the current for three currents (100, 10 and 1 pA columns) and for three bias voltages (2, 4 and 8 V, rows). The corresponding displacements are indicated in the bottom right corners. Colors refer to the particular energy channel the electron is transferring from (as in (b)–(d)). Barrier potential maxima are indicated by the dashed black lines. The numbers specify the partial current in units of electrons per laser pulse for the first and second photocurrent channel. The integration along the energy axis gives the total current for a given distance and bias voltage. The energy axis is given relative to the bias voltage, i.e. the Fermi level in the tip.

$$f_P(E) = \sum_{j=0}^{N} A_j \Bigg/ \left(\exp\left(\frac{E - (eU_B + E_j)}{\Delta E_j} \right) + 1 \right), \tag{4}$$

whereas the tunnel current reveals the general distribution of electrons, it is not necessarily sensitive to the exact locations of the intervals E_j. Thus, for simplicity, we set the energy intervals of $f_P(E)$ to multiples of the photon energy $E_j = j \cdot \hbar\omega$ above the Fermi energy, with integer j and $\hbar\omega = 1.55$ eV. We find that one unexcited ($j = 0$) and two higher-energy contributions ($j = 1, 2$) are fully sufficient to describe the data.

We note that there is no one-to-one correspondence between the energy intervals and the respective one- or two-photon absorption process. Specifically, the observed nonlinear order of 2.5 indicates that other factors, including lower-lying initial states and energy redistribution by thermalization, significantly affect the resulting carrier distribution. The parameters adjusted are the amplitudes A_1 and A_2 relative to A_0 (set to unity), the energy widths ΔE_1 and ΔE_2, and the scaling constant C. The broadening $\Delta E_0 = 7$ meV is set to correspond to the base temperature of 80 K.

Simulation results

The simulations yield a general agreement with the respective experimental curves demonstrating the broad applicability of the model (lines in figures 2(a) and 5(a)). One representative result is presented in figure 4(c) along with the respective occupation function in figure 4(b). Each individual current channel (black lines and colored areas) exhibits an almost ideal exponential decay over all displacements and justifies the previously applied multi-exponential fits. As found before, the short- and long-distance ranges are dominated to nearly 100% by the regular and high-energy contributions (I_2), respectively. The first photocurrent channel (I_1) contributes only in a narrow transition region with a few percent of the total current (figure 4(d)).

We identify the electron energy regions from which the current channels are originating by calculating the product $\Gamma_P(E) = Cf_P(E) \cdot T(E)$, i.e. the integrand of equation (3) (figure 4(e)). Several conclusions can be drawn: (1) While I_2 is the dominant photo-driven current for all bias voltages, the relative fraction I_1 / I_2 becomes more substantial at higher bias voltages. (2) The higher-energy contributions are always close to the potential barrier maximum (extracted from the simulation and indicated by dashed lines in figure 4(e)), which is consistent with the fitted ABH of a few tens of meV. However, there is always a significant above-barrier fraction (up to 80% (0.8 pA) for the 2 V case). (3) The energy bandwidth (FWHM) of the channels is of the order of 0.5 eV
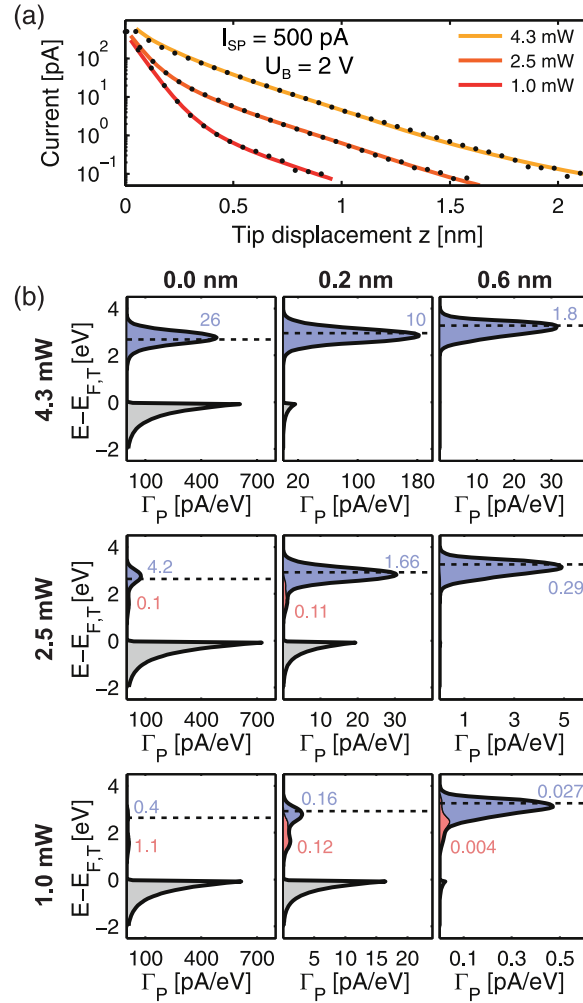
Figure 5. (a) Three examples of the experimental $I(z)$ curves (black dots) for the average laser powers of 1.0, 2.5 and 4.3 mW and the corresponding simulation results (solid lines). (b) Representations of the energetic composition of the current for three distances (0.0, 0.2 and 0.6 nm, columns) and for the three average laser powers in (a) (rows). Note the changing of the x-axis scaling. As in figure 4(e) colors assign to the current channels: regular tunneling (gray), first (magenta) and second (blue) photocurrent contribution. Barrier potential maxima are indicated by the dashed black lines. The numbers indicate the partial current in the unit of electrons per laser pulse.

and 0.8–1.5 eV for regular tunneling and photocurrent, respectively. (4) Field emission and scattering resonances enforce the appearance of a modulated contour evident by multiple peaks and shoulders around the potential barrier maxima for larger distances and higher bias voltages (compare, e.g. 4.0 and 8.0 V for 1 pA).

Analyzing the current composition as a function of laser power[6] (figure 5(b)) shows that I_1 has a significant contribution for lower laser powers. The average charge transferred per channel can be increased up to a few tens of electrons per laser pulse by increasing the incident power (indicated as numbers in figures 4(e) and 5(b)).

Discussion

The results presented in this paper, specifically the determination of the effective electron distributions, yield insights into the transport mechanism responsible for photocurrents in STM under fs-laser illumination. The main experimental features are reproduced, and the findings suggest multiphoton absorption processes leading to the population of higher-energy electron states (hot electrons) close to the potential barrier maximum. Open questions involve the possible participation of higher-order photon absorption, the role of lower-energy initial states (d-band), and transfer rate modifications due to quantum coupling of electronic states (quenching of radiative resonances).

---

[6] Note that here we use constant displacements instead of constant currents (as in figure 4(e)). The z-shift corrections Δz are of minor magnitude and, therefore, currents at a constant tip displacement are comparable.

As former studies demonstrated, thermally induced tip expansion due to the pulsed illumination have been a major issue for combining STM and fs-laser excitation, since they can obscure the electronic signal by the oscillatory altering of the gap width by a certain amount of $\delta z_{\exp}(t)$ and its strong impact on the exponential tunnel current [1]. The tip expansion can result in a mechanical tip-sample contact, which causes instabilities and tip and sample structuring [72]. However, for the low laser fluences used in this experiment, we can neglect any contact formation (as demonstrated in figure 3). The magnitude of $\delta z_{\exp}(t)$ can be estimated from theoretical and experimental studies, which demonstrate monotonically decreasing values for high repetition rates[7] [73, 74]. In addition, by assuming an exponential current-distance relation $I(z, t) \sim \exp(-2\kappa[z + \delta z_{\exp}(t)])$ we see that for the measured time-averaged signal,

$$< I(z, t) >_t = <\exp(-2\kappa\delta z_{\exp}(t)) >_t I(z) = c_{\exp}I(z), \qquad (5)$$

only a modification of the amplitude by a constant factor $c_{\exp} \approx 1$ is present (assuming $\delta z_{\exp}(t)$ independent of z). Hence, an oscillatory tip expansion $\delta z_{\exp}(t)$ cannot explain the found reduced ABH.

We conducted several validation experiments that exclude a strong thermal impact on the observed current-distance dependencies. First of all, the negative bias measurements (figure A4 in the appendix 'Bias voltage dependent measurements') show a strong rectification effect, i.e. even for negative setpoint currents (electron transfer to the tip) we find a positive current contribution (electron transfer to the sample) when retracting the tip out of the regular tunneling regime. Secondly, we do not find any signal for laser s-polarization. Finally, the signal is confined to an area that is a factor of 5–6 smaller than the focal spot size (demonstrated by the focal scan in the left inset of figure 1(c)). This is a strong indication of the nonlinearity of the photo-driven current and contradicts a thermal expansion effect which, in contrast, is expected to be governed by linear absorption.

Our experiments have been operated in the perturbative regime with low-order nonlinear transitions. By contrast, strong-field effects are expected to play a major role for laser powers increased by about a factor of 10 compared to those in our experiments [36, 64]. Performing STM measurements under such conditions, laser-power-dependent ABHs have been observed [55]. In the limit of much lower intensities, continuous-wave illumination may change the transfer mechanism to plasmon-assisted resonant tunneling, as recently demonstrated by FER shifts of one photon energy [84]. We do not observe such shifts, presumably due to a broader electron energy distribution and the smaller photo-driven contribution to the total current (see figure A5 in the appendix 'Bias voltage dependent measurements').

Both the experimental and theoretical approach can be further extended. On the one hand, pump-probe schemes have the potential to give access to the temporal evolution of the electron distribution [85]. On the other hand, additional modeling, including the distance dependent plasmonic field, electronic band structures, the three-dimensional transient field distribution as well as the relaxation dynamics (Landau damping, electron–electron and electron-phonon scattering) promise further information on the specific electronic pathways under fs illumination [86, 87].

Conclusion

In conclusion, we demonstrated photo-driven electron transfer through the tunnel junction of a scanning tunneling microscope. Under gap illumination, this current is evident by tip retraction curves with additional contributions distinguished by a strongly reduced apparent barrier height leading to a long decaying current compared to regular tunneling. The analysis of power dependent measurements suggests a multiphoton absorption mechanism where the electrons are excited to levels a few 100 of meV around the potential barrier maximum. Neither the laser power nor the bias voltage strongly affects the ABH in the measured range. The electron excitation to the high energies is provided by the plasmonically enhanced field, albeit its distance dependency does not explain the observed decay length scales. Simulations based on a one-dimensional potential barrier model and a time-averaged effective electron occupation are able to reproduce the central features of the current-distance dependencies. By this, we identify the involved energy domains from which the transfer channels are established and find a high-energy distribution in the vicinity of the potential barrier maximum to be the dominant contribution. Prospectively, this could provide an ultrafast excitation procedure with high-energy electrons in a nearly field-free environment, e.g. to disentangle field- and particle-driven chemical reactions of molecules.

---

[7] Most of the presented data was measured with laser average powers between 1 and 10 mW. The resulting fluences are several magnitudes below the contact formation threshold given in [72]. Moreover, the amplitude of the oscillating tip expansion is expected to be in the sub-Ångström regime as estimated from theoretical and experimental studies [73, 74].

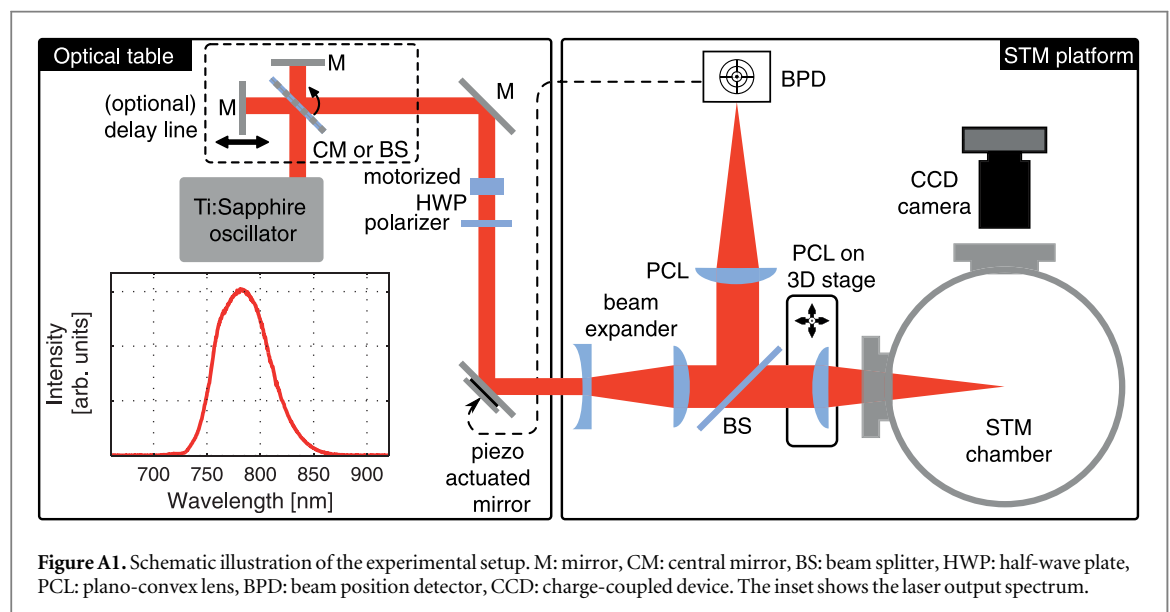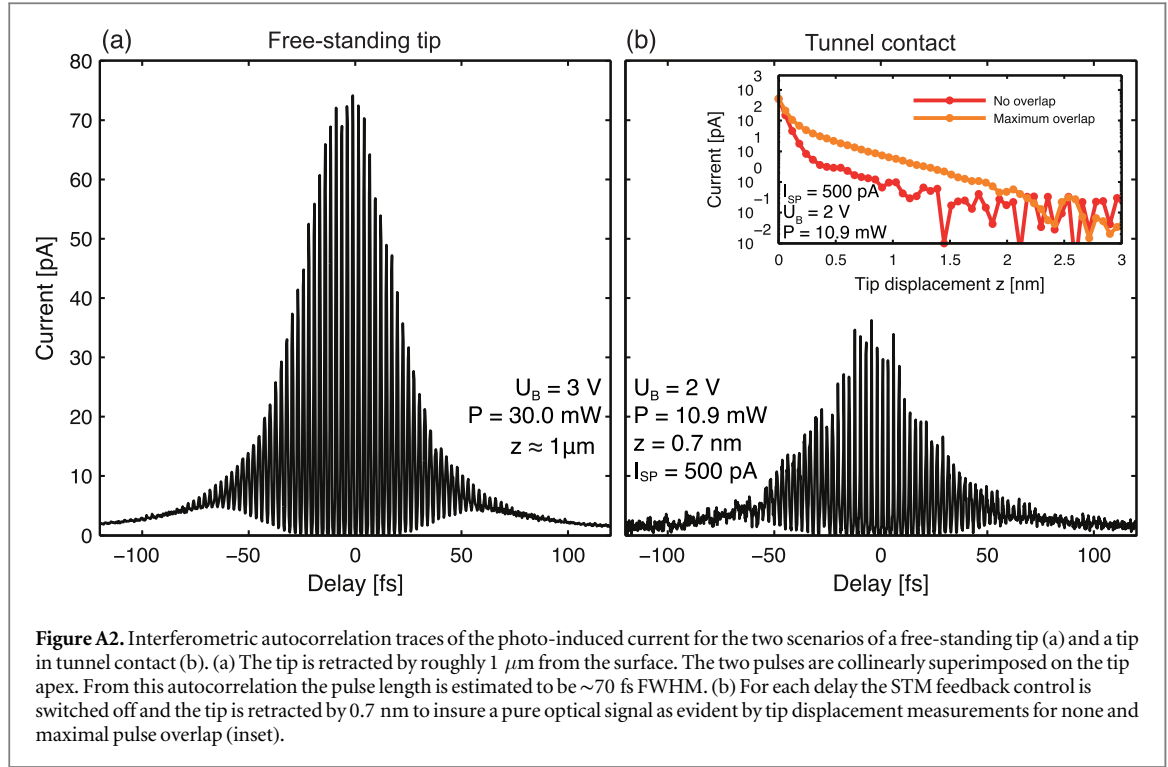## Acknowledgments

Appendix

A.1. Methods

A.1.1. Experimental setup. Figure A1 illustrates the experimental setup. A Titanium-Sapphire laser oscillator (Coherent Vitara T-HP) provides laser pulses with 80 MHz repetition rate. The laser spectrum has a center wavelength of 785 nm and a bandwidth of 60 nm (see spectrum in the inset). A pair of a remotely rotatable half-wave plate and a film polarizer is used to set the laser polarization and average power. The polarization is chosen to be p-polarized (aligned along the tip's symmetry axis), unless otherwise stated. The beam width is increased by a factor of five with a telescope arrangement resulting in a focus diameter of 18 μm in the STM after passing a plano-convex lens ($f = 200$ mm). A precise positioning and raster scanning of the focus is achieved by remotely moving the focusing lens with a 3D-translation stage.

An active beam stabilization system consisting of a beam position detector on the STM platform and a piezo actuated mirror on the optical table is implemented to prevent pointing caused by the relative movement between both table and platform. Optionally a Michelson-type interferometer can be inserted into the beam line by replacing the central mirror with a 90° turned beam splitter (dashed section in figure A1). With this we estimated the pulse duration to be 70 fs in the STM chamber from autocorrelation traces (see appendix 'Interferometric autocorrelation').

We used a home-built UHV scanning tunneling microscope with 5×10^{-11} mbar of base pressure for the experiments. The system is cooled with liquid nitrogen down to 80 K. Currents are converted to voltage signals by an *I–V*-converter (1 V nA^{-1}) with a bandwidth of 1 kHz. Hence, the STM feedback control is not affected by the 80 MHz modulation of the laser oscillator and only a time averaged signal is recorded. The bias voltage is connected to the sample, while the tip is grounded. Viewports allow for an optical access for the laser illumination and the monitoring of the tip and focus position via a CCD camera (figure 1(a)).

A.1.2. Tip and sample preparation. Gold wires (250 μm in diameter) are annealed in vacuum with 750 °C for several hours. This increases the mean grain size and leads to quasi-single-crystalline apex sections for the final tips. Afterwards a tapered end is achieved by electrochemical etching with 37% hydrochloric acid and subsequently the tips are cleaned with iso-2-propanol and distilled water. Shape and surface quality as well as apex radii are checked by scanning electron microscopy (details e.g. in [60, 88]). Moderate annealing at 150 °C for 72 h is conducted to clean the tip surface in the UHV during a preparation chamber bake-out. Cu(100)

Figure A1. Schematic illustration of the experimental setup. M: mirror, CM: central mirror, BS: beam splitter, HWP: half-wave plate, PCL: plano-convex lens, BPD: beam position detector, CCD: charge-coupled device. The inset shows the laser output spectrum.

Figure A2. Interferometric autocorrelation traces of the photo-induced current for the two scenarios of a free-standing tip (a) and a tip in tunnel contact (b). (a) The tip is retracted by roughly 1 μm from the surface. The two pulses are collinearly superimposed on the tip apex. From this autocorrelation the pulse length is estimated to be ~70 fs FWHM. (b) For each delay the STM feedback control is switched off and the tip is retracted by 0.7 nm to insure a pure optical signal as evident by tip displacement measurements for none and maximal pulse overlap (inset).

treatment comprises multiple cycles of argon ion sputtering (700 V) and annealing (350 °C–400 °C) of single crystals. Finally, 0.1–0.2 monolayers of germanium have been evaporated by electron beam evaporation.

A.2. Apparent barrier height

In general, the work function of a material is the central quantity defining the potential barrier for an electron that transfers from the cathode to the anode. For sub-nanometer gaps between both electrodes this barrier is strongly modified in its shape and height. In this case, the characteristic quantity of electron transport is the apparent barrier height (ABH) which is a measure of the effective potential:

$$\Phi_{\mathrm{ABH}}(z) = \frac{\hbar^2}{8m_e}\left(\frac{d\ln I}{dz}\right)^2, \tag{A1}$$

where m_e is the electron mass [61]. For an exponential current representation ($I(z) \sim \exp(-2\kappa z)$) the ABH simplifies to $\Phi_{\mathrm{ABH}} = \hbar^2\kappa^2/2\,m_e$, with the decay constant κ.

A.3. Start point correction

In conventional STM, the absolute tip-sample distance z_0 is determined by the parameters bias voltage U_{B} and setpoint current I_{SP}. In our experiments, the start point is also a function of the laser power P, since the photo-driven signal has a pronounced tip-sample distance dependency. We take this circumstance into account by introducing a distance $\Delta z > 0$. Qualitatively, for a given distance, the current increases when increasing U_{B} or P and, in conclusion, the tip has to be retracted by Δz from the sample in order to keep the setpoint current constant.

In our experiments, we did power $I_{\mathrm{P}}(z)$ and voltage $I_{U_{\mathrm{B}}}(z)$ dependent measurements for given setpoint currents and corrected the data sets by extracting $\Delta z(P)$ from the bi-exponential fits and by using a separate $\Delta z(U_{\mathrm{B}})$ measurement for the power and bias voltage dependent measurements, respectively (figures 1(b) and 2(a)). While a minor correction of 0.05 nm is determined for the highest laser power compared to the lowest one, $\Delta z = 1.2$ nm is found for a voltage change from 2 to 8 V (see top inset of figure 2(a)).

A.4. Interferometric autocorrelation

We measured interferometric autocorrelation traces for the two scenarios of a free-standing tip (~1 μm tip-sample distance) and for tunnel contact (figures A2(a) and (b)) by utilizing double pulses with a variable delay provided by a Michelson-type interferometer (see appendix A.1). Both interferometer arms have the same laser average power and are collinearly interfering at the apex or at the tunnel junction. In order to measure only the photo-driven current, the tip is retracted at each delay step by 0.7 nm with respect to the setpoint (no regular tunneling) and the photocurrent is recorded. $I(z)$ curves demonstrate for a maximal pulse overlap and without
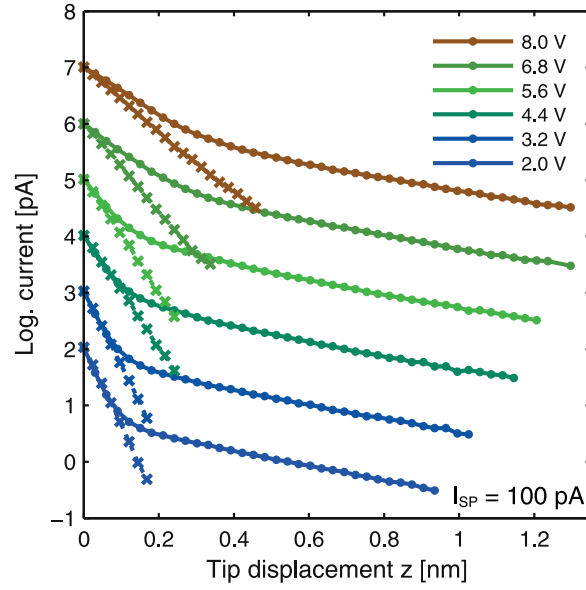
Figure A3. Comparison of current-distance dependencies with (dots) and without (crosses) illumination of the tunnel junction for six different bias voltages. In the former case the average laser power is $P = 3.4$ mW (same data as in figure 2(a)). The y-axis has a logarithmic scale. For clarity the curves are shifted vertically and only data points exceeding the noise level are plotted. For simplicity, no displacement correction due to different start points is applied.
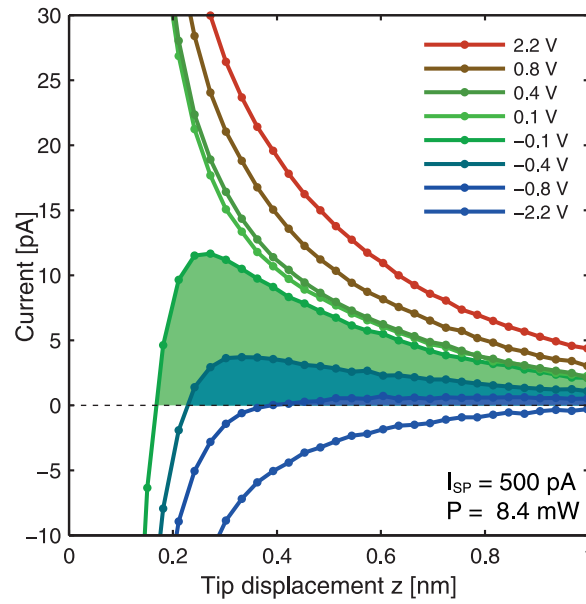

Figure A4. Tip-distance dependencies for positive and negative bias voltages ranging from -2.2 to 2.2 V. The data were measured with laser excitation ($P = 8.4$ mW) and a setpoint current of 500 pA. Importantly, $I(z)$ curves for negative bias voltages show a pronounced positive current regime (shaded areas) evidencing electron transport from the tip to the sample, despite the negative setpoint. This rectification effect is clearly observable for bias voltages down to -1 V. At some point, a negative photocurrent contribution originating from the sample surface conceals the positive current from the tip resulting in a negative net photocurrent. For visibility, only a segment of the actual measured range is shown (no displacement correction is applied).

a pulse overlap that the photocurrent is finite and regular tunneling is dominant providing a quasi-constant reference distance z_0 at each delay step (see inset in figure A2(b)). As in the power dependent measurement in figure 2, the setpoint distance z_0 only varies in a sub-Ångström regime for different delays.

From the traces we found peak-to-background ratios (PBR) of $\sim$68 and $\sim$31 for the free-standing tip and for tunnel contact, respectively, which indicates the high nonlinearity n of both situations: under ideal experimental conditions the PBR is equal to 2^{2n-1}. This implies an effective nonlinearity of $n = 3.54$ for the free-standing tip and $n = 2.97$ for the tunnel contact. These values are within the variations, which we observed in the power dependent measurements and support that we have a lower nonlinear order in the tunnel contact compared to a
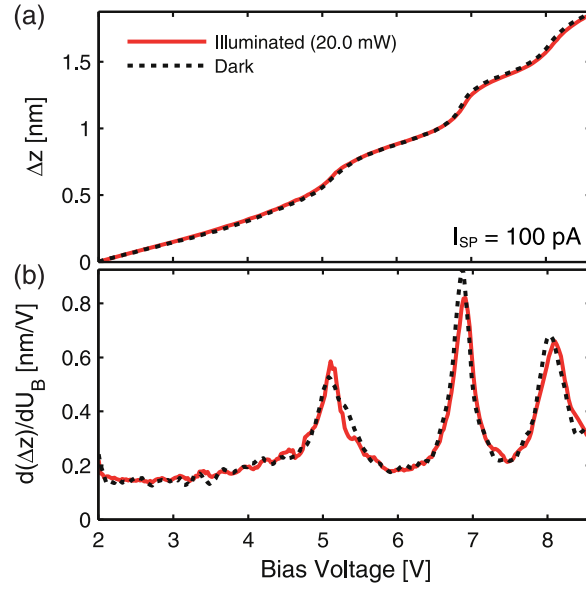
Figure A5. (a) Tip retraction, i.e. start position change, as a function of bias voltage in the range of 2.0–8.6 V with (solid red line) and without (dashed black line) optical excitation of the tunnel junction. The current was kept constant at 100 pA. (b) The derivative with respect to the bias voltage of the curves in (a). Image potential states are evident by the three peaks at 5.0, 6.9 and 8.0 V. Apparently, the fs-laser pulses do not have a strong impact on the curves, especially, the position and shape of the field emission resonances are unaffected.
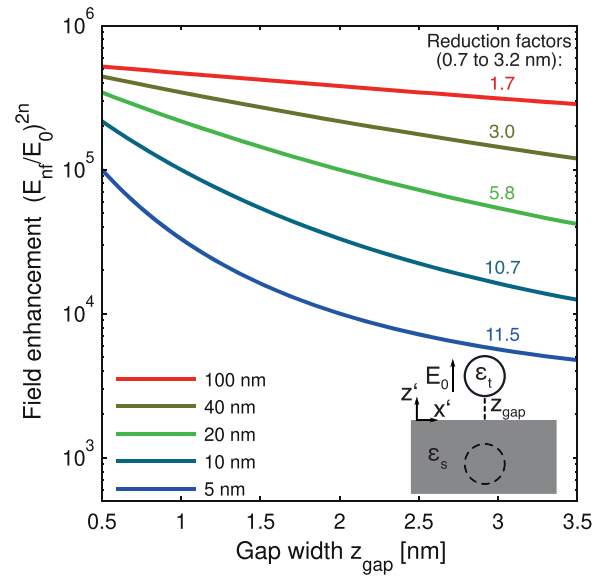
Figure A6. Distance dependency of the plasmonic field enhancement (gap plasmon) $(E_{nf}/E_0)^{2n}$ calculated with a coupled dipole approximation for tip radii between 5 and 100 nm. Dielectric functions for the gold tip (ε_t) and copper sample (ε_s) for a wavelength of 785 nm have been taken from [89]. Note that we incorporated the nonlinear order of $n = 2.5$ extracted from the experimental data. The numbers indicate the reduction factor between 0.7 and 3.2 nm, which is the experimentally investigated interval.

free-standing tip. The value of $n \approx 3$ for the tunnel contact might be somewhat overestimated due to thermal tip expansion changes induced by the intensity oscillations in the interfering pulses.

A.5. Bias voltage dependent measurements

A.5.1. Field emission resonances.   A well-known phenomenon for large bias voltages U_B is the contribution of image states in front of the surface of a conducting sample to the tunneling current [68, 69, 71, 90] (see $\Delta z (U_B)$ spectra in figures 2(a) and A5). These field emission resonances (FER) are characterized by an increased conductivity for the bias voltage matching the FER energy [91]. Considering a V-shaped potential landscape, such as an image potential, the corresponding electronic states exhibit a hydrogen-like energy spectrum [92].
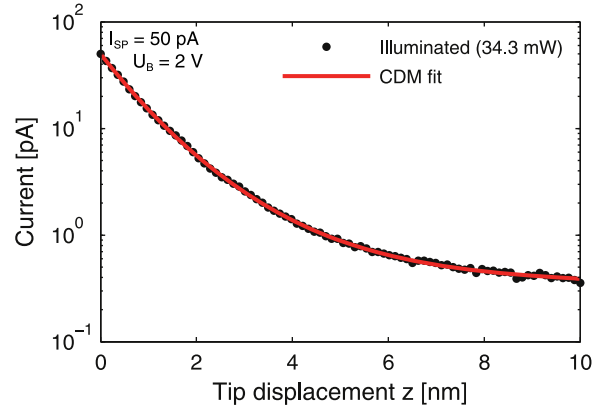
Figure A7. Current-distance dependency (black dots) for higher-power apex illumination (34.3 mW). The observed current decay length is much longer compared to the low-power measurements in figures 1 and 2. At large displacements the current converges to an effective constant value of 0.4 pA. Importantly, there is no regular tunneling at the setpoint value. The coupled dipole model (CDM) fits a nonlinear order of $n = 4.4 \pm 0.2$ and a tip radius of 28 ± 2 nm (red line).
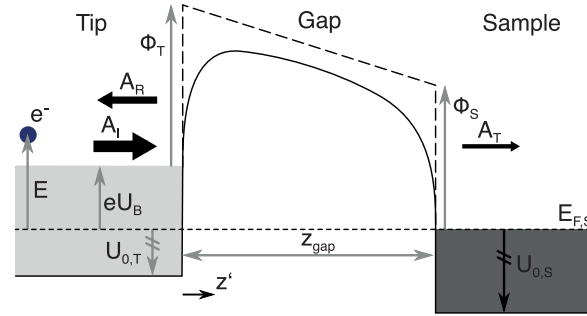

Figure A8 Scheme of the one-dimensional potential barrier model used for the calculation of the electron transmission probability. The complex amplitudes of the incoming A_I, reflected A_R and transmitted A_T wave function are illustrated as black arrows. The applied values for the work functions and inner potentials of tip and sample are listed in table A1.

Table A1. The material parameters used for the transmission probability simulation.

Name	Symbol	Value
Sample work function	Φ_S	4.5 eV
Sample inner potential	$U_{0,S}$	-7.0 eV
Tip work function	Φ_T	5.1 eV
Tip inner potential	$U_{0,T}$	-9.2 eV
Sample Fermi energy	$E_{F,S}$	0 eV

STM studies found a modification of the image potential energies due to the Stark shift caused by the static electric field between tip and sample [68, 70].

The FER appear at bias voltages of 5.0, 6.6, and 7.7 V, as evident from the peaks in the $\mathrm{d}(\Delta z(U_B))/\mathrm{d}U_B$ spectrum (bottom inset of figure 2(a)). The increased conductivity at the resonances causes slight deviations from the typical exponential form in the regular tunneling regime (e.g. 6.8 and 8.0 V in figure 2(a)). The potential sensitivity of the FER spectrum (and as a consequence the dependency from the tip-sample distance) qualitatively explains the curve shape deviations.

A.6. Near-field enhancement

The electromagnetic field enhancement of a tip-sample system illuminated with a plane wave E_0 propagating in x'-direction and polarized along the z'-direction (inset figure A6) can be modeled with a sphere of radius R_T representing the tip apex in front of a surface. The electromagnetic response of the sphere is described by a dipole

moment. This, in turn, induces its image dipole in the sample from which an effective dipole moment can be calculated [80]. The superposition of both dipolar fields with the incident plane wave gives the total field distribution [93]. Evaluating the field at the tip apex ($x' = 0$, $z' = z_{gap}$) delivers an algebraic relation for the z'-component of the total field $E_{nf} \sim (z_{gap} + R_T)^{-3}$ [29]. Figure A6 presents the tip-sample distance dependency calculated with the coupled dipole model (CDM) for a nonlinear process ($\sim |E_{nf}|^{2n}$) of the order of $n = 2.5$ and tip radii between 5 and 100 nm.

A.7. Transport model

For the calculation of the transmission probability T, a one-dimensional barrier model, composed of the three regions (tip, gap and sample) is used (figure 4(a) and figure A8). The tip and sample are assumed to be field free, i.e. constant potentials of $U_{0,T} + eU_B$ and $U_{0,S}$ for the tip and sample ($U_{0,j}$ is the inner potential), respectively. The total potential $V(z')$ inside the gap is the result of the superposition of the image potentials for both tip and sample, and the linear potential drop due to the bias voltage and the work function differences. Effective surface positions for the tip and sample are applied to fulfill continuous boundary conditions at $z' = 0$ and $z' = z_{gap}$ [91, 94]. Within a scattering approach, the Schrödinger equation is solved numerically by the Numerov method with the usual assumption of continuously differentiable wave function transitions [82, 91]. From the complex wave function amplitudes the transmission probability is calculated [83]. A schematic illustration of the real part of a wave function is given in figure 4(a): regions with $E > V(z')$ (tip and sample) are characterized by an oscillatory waveform while the wave function inside the gap ($E < V(z')$) decays exponentially.

Both, tip and sample material, are assumed to have a constant local density of states. The sample temperature is set to 0 K.

The optimization procedure of the free parameters in the effective occupation function was implemented in Matlab. In advance, the absolute gap width z_0 was fitted for a representative data set and has been fixed for all following simulation iterations. In addition, a slight offset of the order of a few tens to a few hundreds of meV was added to the energy intervals E_j in order to match the actual work function of the tip. We found that the energy widths ΔE_1 and ΔE_2—corresponding to the temperature of the two photo-driven contributions to the effective occupation distribution—attain values of several tens to a few hundreds of meV, which is equivalent to 1000–2000 K. These high values are necessary to somewhat flatten out the effects of scattering and field emission resonances.

ORCID iDs

Benjamin Schröder ⓘ https://orcid.org/0000-0002-7383-0406
Ole Bunjes ⓘ https://orcid.org/0000-0002-4792-4169
Lara Wimmer ⓘ https://orcid.org/0000-0002-2209-0209
Katharina Kaiser ⓘ https://orcid.org/0000-0001-7519-8005
Georg A Traeger ⓘ https://orcid.org/0000-0003-4286-7895
Thomas Kotzott ⓘ https://orcid.org/0000-0002-5986-5207
Claus Ropers ⓘ https://orcid.org/0000-0002-9539-3817
Martin Wenderoth ⓘ https://orcid.org/0000-0001-9663-3512

References

[1] Grafström S 2002 *J. Appl. Phys.* **91** 1717
[2] Gerstner V, Knoll A, Pfeiffer W, Thon A and Gerber G 2000 *J. Appl. Phys.* **88** 4851
[3] Shigekawa H and Yoshida S 2018 *AAPPS Bull.* **28** 9
[4] Tian Y, Yang F, Guo C and Jiang Y 2018 *Surf. Rev. Lett.* **25** 1841003
[5] Kazuma E, Jung J, Ueba H, Trenary M and Kim Y 2018 *Prog. Surf. Sci.* **93** 163
[6] Mehlhorn M, Carrasco J, Michaelides A and Morgenstern K 2009 *Phys. Rev. Lett.* **103** 1
[7] Mehlhorn M, Gawronski H and Morgenstern K 2010 *Phys. Rev. Lett.* **104** 076101
[8] Böckmann H, Liu S, Mielke J, Gawinkowski S, Waluk J, Grill L, Wolf M and Kumagai T 2016 *Nano Lett.* **16** 1034
[9] Li S, Chen S, Li J, Wu R and Ho W 2017 *Phys. Rev. Lett.* **119** 176002
[10] Böckmann H, Gawinkowski S, Waluk J, Raschke M B, Wolf M and Kumagai T 2018 *Nano Lett.* **18** 152
[11] Li S, Czap G, Wang H, Wang L, Chen S, Yu A, Wu R and Ho W 2019 *Phys. Rev. Lett.* **122** 077401
[12] Böckmann H, Müller M, Hammud A, Willinger M G, Pszona M, Waluk J, Wolf M and Kumagai T 2019 *J. Phys. Chem. Lett.* **10** 2068
[13] Kazuma E, Jung J, Ueba H, Trenary M and Kim Y 2018 *Science* **360** 521
[14] Bartels L, Wang F, Möller D, Knoesel E and Heinz T F 2004 *Science* **305** 648
[15] Lee J, Perdue S M, Rodriguez Perez A and Apkarian V A 2014 *ACS Nano* **8** 54
[16] Cocker T L, Peller D, Yu P, Repp J and Huber R 2016 *Nature* **539** 263
[17] Imada H, Miwa K, Imai-Imada M, Kawahara S, Kimura K and Kim Y 2017 *Phys. Rev. Lett.* **119** 1
[18] Kröger J, Doppagne B, Scheurer F and Schull G 2018 *Nano Lett.* **18** 3407
[19] Mehlhorn M, Gawronski H, Nedelmann L, Grujic A and Morgenstern K 2007 *Rev. Sci. Instrum.* **78** 033905

[20] Wu S W, Ogawa N and Ho W 2006 *Science* **312** 1362

[21] Wu S W and Ho W 2010 *Phys. Rev.* B **82** 085444

[22] Terada Y, Yoshida S, Takeuchi O and Shigekawa H 2010 *Nat. Photon.* **4** 869

[23] Yoshida S, Terada Y, Oshima R, Takeuchi O and Shigekawa H 2012 *Nanoscale* **4** 757

[24] Kloth P, Kaiser K and Wenderoth M 2016 *Nat. Commun.* **7** 10108

[25] Kloth P and Wenderoth M 2017 *Sci. Adv.* **3** e1601552

[26] Sun L, Dong A, Li J, Hao D, Tang X, Yan S, Guo Y, Shan X and Lu X 2018 *Phys. Rev.* B **98** 081402

[27] Zhang R *et al* 2013 *Nature* **498** 82

[28] Chen C, Hayazawa N and Kawata S 2014 *Nat. Commun.* **5** 3312

[29] Kravtsov V, Berweger S, Atkin J M and Raschke M B 2014 *Nano Lett.* **14** 5270

[30] Jiang S, Zhang Y, Zhang R, Hu C, Liao M, Luo Y, Yang J, Dong Z and Hou J G 2015 *Nat. Nanotechnol.* **10** 865

[31] Lee J, Tallarida N, Chen X, Jensen L and Apkarian V A 2018 *Sci. Adv.* **4** eaat5472

[32] Lee J, Crampton K T, Tallarida N and Apkarian V A 2019 *Nature* **568** 78

[33] Cocker T L, Jelic V, Gupta M, Molesky S J, Burgess J A J, Reyes G D L, Titova L V, Tsui Y Y, Freeman M R and Hegmann F A 2013 *Nat. Photon.* **7** 620

[34] Kloth P, Thias T, Bunjes O, von der Haar J and Wenderoth M 2016 *Rev. Sci. Instrum.* **87** 123702

[35] Takeuchi O, Mogi H, Wang Z, Yoon C H, Taninaka A, Yoshida S and Shigekawa H 2019 *Japan. J. Appl. Phys.* **58**

[36] Garg M and Kern K 2019 *Science* **367** 411

[37] Pfeiffer W, Sattler F, Vogler S, Gerber G, Grand J-Y and Möller R 1997 *Appl. Phys* B **64** 265–8

[38] Khusnatdinov N N, Nagle T J and Nunes G 2000 *App. Phys. Lett.* **77** 4434–6

[39] Yoshida S, Hirori H, Tachizaki T, Yoshioka K, Arashida Y, Wang Z-H, Sanari Y, Takeuchi O, Kanemitsu Y and Shigekawa H 2019 *ACS Photonics* **6** 1356–64

[40] Gimzewski J K, Sass J K, Schlitter R R and Schott J 1989 *Europhys. Lett.* **8** 435

[41] Berndt R, Gimzewski J K and Johansson P 1991 *Phys. Rev. Lett.* **67** 3796

[42] Bischoff M M, van der Wielen M C M and van Kempen H 1998 *Surf. Sci.* **400** 127

[43] Nilius N, Ernst N and Freund H-J 2002 *Phys. Rev.* B **65** 1

[44] Schull G, Néel N, Johansson P and Berndt R 2009 *Phys. Rev. Lett.* **102** 1

[45] Yu A, Li S, Wang H, Chen S, Wu R and Ho W 2018 *Nano Lett.* **18** 3076

[46] Zhang L *et al* 2017 *Nat. Commun.* **8** 580

[47] Rosławska A, Merino P, Große C, Leon C C, Gunnarsson O, Etzkorn M, Kuhnke K and Kern K 2018 *Nano Lett.* **18** 4001

[48] Leon C C, Rosławska A, Grewal A, Gunnarsson O, Kuhnke K and Kern K 2019 *Sci. Adv.* **5** eaav4986

[49] Gerstner V, Thon A and Pfeiffer W 2000 *J. Appl. Phys.* **87** 2574

[50] Takeuchi O, Morita R, Yamashita M and Shigekawa H 2002 *Japan. J. Appl. Phys.* **41** 4994

[51] Aoyama O T M, Oshima R, Okada Y, Oigawa H, Sano N, Shigekawa H, Morita R and Yamashita M 2004 *Appl. Phys. Lett.* **85** 3268

[52] Dolocan A, Acharya D P, Zahl P, Sutter P and Camillone N 2011 *J. Phys. Chem.* C **115** 10033

[53] Meng X, Jin W, Yang H, Dadap J I, Osgood R M, Dolocan A, Sutter P and Camillone N 2017 *Opt. Lett.* **42** 2651

[54] Lee J, Perdue S M, Whitmore D and Apkarian V A 2010 *J. Chem. Phys.* **133** 104706

[55] Dey S, Mirell D, Perez A R, Lee J and Apkarian V A 2013 *J. Chem. Phys.* **138** 154202

[56] Ropers C, Neacsu C C, Elsaesser T, Albrecht M, Raschke M B and Lienau C 2007 *Nano Lett.* **7** 2784

[57] Berweger S, Atkin J M, Olmon R L and Raschke M B 2010 *J. Phys. Chem. Lett.* **1** 3427

[58] Schröder B, Sivis M, Bormann R, Schäfer S and Ropers C 2015 *Appl. Phys. Lett.* **107** 231105

[59] Schröder B *et al* 2015 *Phys. Rev.* B **92** 085411

[60] Schmidt S, Piglosiewicz B, Sadiq D, Shirdel J, Lee J S, Vasa P, Park N, Kim D-S and Lienau C 2012 *ACS Nano* **6** 6040

[61] Chen C J 2008 *Introduction to Scanning Tunneling Microscopy* 2nd edn (New York: Oxford University Press)

[62] Ropers C, Solli D R, Schulz C P, Lienau C and Elsaesser T 2007 *Phys. Rev. Lett.* **98** 043907

[63] Ropers C, Elsaesser T, Cerullo G, Zavelani-Rossi M and Lienau C 2007 *New J. Phys.* **9** 397

[64] Bormann R, Gulde M, Weismann A, Yalunin S V and Ropers C 2010 *Phys. Rev. Lett.* **105** 147601

[65] Vogelsang J, Robin J, Nagy B J, Dombi P, Rosenkranz D, Schiek M, Groß P and Lienau C 2015 *Nano Lett.* **15** 4685

[66] Müller M, Kravtsov V, Paarmann A, Raschke M B and Ernstorfer R 2016 *ACS Photonics* **3** 611

[67] Girardeau-Montaut J P and Girardeau-Montaut C 1995 *Phys. Rev.* B **51** 13560

[68] Binnig G, Frank K H, Fuchs H, Garcia N, Reihl B, Rohrer H, Salvan F and Williams A R 1985 *Phys. Rev. Lett.* **55** 991

[69] Ploigt H, Brun C, Pivetta M, Patthey F and Schneider W 2007 *Phys. Rev.* B **76** 195404

[70] Martínez-Blanco J and Fölsch S 2015 *J. Phys.: Condens. Matter* **27** 255008

[71] Kumagai T, Liu S, Shiotari A, Baugh D, Shaikhutdinov S and Wolf M 2016 *J. Phys. Condens. Matter* **28**

[72] Boneberg J, Münzer H J, Tresp M, Ochmann M and Leiderer P 1998 *Appl. Phys.* A **67** 381

[73] Grafström S, Schuller P, Kowalski J and Neumann R 1998 *J. Appl. Phys.* **83** 3453

[74] Xie N, Gong H, Yan S, Zhao J, Shan X, Guo Y, Sun Q and Lu X 2012 *Appl. Phys. Lett.* **101** 213104

[75] Yanagisawa H, Hengsberger M, Leuenberger D, Klöckner M, Hafner C, Greber T and Osterwalder J 2011 *Phys. Rev. Lett.* **107** 087601

[76] Bharadwaj P, Bouhelier A and Novotny L 2011 *Phys. Rev. Lett.* **106** 226802

[77] Becker S F, Esmann M, Yoo K, Groß P, Vogelgesang R, Park N and Lienau C 2016 *ACS Photonics* **3** 2235b00438

[78] Sadiq D, Shirdel J, Lee J S, Selishcheva E, Park N and Lienau C 2011 *Nano Lett.* **11** 1609

[79] Neacsu C C, Berweger S, Olmon R L, Saraf L V, Ropers C and Raschke M B 2010 *Nano Lett.* **10** 592

[80] Knoll B and Keilmann F 2000 *Opt. Commun.* **182** 321

[81] Zhu W, Esteban R, Borisov A G, Baumberg J J, Nordlander P, Lezec H J, Aizpurua J and Crozier K B 2016 *Nat. Commun.* **7** 11495

[82] Numerov B and Nachrichten A 1927 *Astron. Nachr.* **230** 359

[83] Cohen-Tannoudji C, Diu B and Laloe F 2019 *Quantum Mechanics: Volume I: Basic Concepts, Tools, and Applications* 2nd edn (New York: Wiley)

[84] Liu S, Wolf M and Kumagai T 2018 *Phys. Rev. Lett.* **121** 226802

[85] Bauer M, Marienfeld A and Aeschlimann M 2015 *Prog. Surf. Sci.* **90** 319–76

[86] Brongersma M L, Halas N J and Nordlander P 2015 *Nat. Nanotechnol.* **10** 25

[87] Hohlfeld J, Wellershoff S-S, Güdde J, Conrad U, Jähnke V and Matthias E 2000 *Chem. Phys.* **251** 237

[88] Neacsu C C, Berweger S and Raschke M B 2007 *NanoBiotechnology* **3** 172

[89] Johnson P B and Christy R W 1972 *Phys. Rev.* B **6** 4370

[90] Echenique P M, Pitarke J M, Chulkov E V and Silkin V M 2002 *J. Electron Spectros. Relat. Phenomena* **126** 163
[91] Bono J and Good R H 1987 *Surf. Sci.* **188** 153
[92] Chulkov E V, Silkin V M and Echenique P M 1999 *Surf. Sci.* **437** 330
[93] Novotny L and Hecht B 2006 *Principles of Nano-Optics* 1st edn (Cambridge: Cambridge University Press)
[94] Teague E C 1986 *J. Res. Natl Bur. Stand.* 1934 **91** 171